Microstructure and mechanical properties of additively manufactured AlSi10Mg lattice structures from single contour exposure

Marcel Sos [a,c,*], Guillaume Meyer [b,c], Karsten Durst [a,c], Christian Mittelstedt [b,c], Enrico Bruder [a,c]

[a] *Technische Universität Darmstadt, Fachgebiet Physikalische Metallkunde, Alarich-Weiss-Straße 2, 64287 Darmstadt, Germany*
[b] *Technische Universität Darmstadt, Fachgebiet Konstruktiver Leichtbau und Bauweisen, Otto-Berndt-Straße 2, 64287 Darmstadt, Germany*
[c] *Additive Manufacturing Center, Technische Universität Darmstadt, 64287 Darmstadt, Germany*

HIGHLIGHTS

- An additional degree of freedom in the microstructural design of filigree struts manufactured via single contour exposure was shown.
- A schematical model based on local overheating is presented to explain gradients in texture, grain size and silicon cell size.
- The macroscopic mechanical properties of lattices were switched from brittle to ductile after heat treatment for 2 h at 350 °C.
- Microstructural and geometrical influences on lattice deformation and failure modes were investigated, showing that unit cell geometry is the dominant factor.

GRAPHICAL ABSTRACT
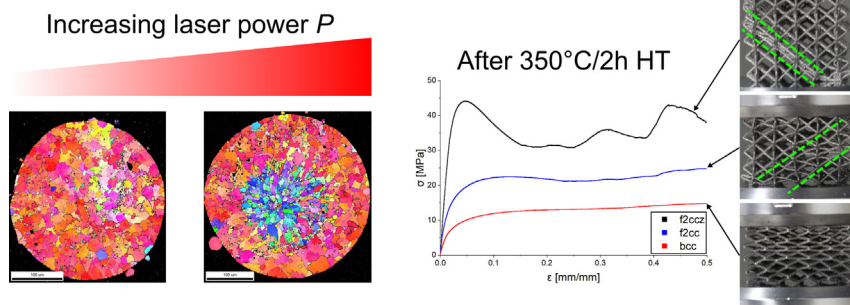
ARTICLE INFO

ABSTRACT

Metal-based additive manufacturing techniques offer the ability to produce complex, near net shape parts that would be impossible or prohibitively expensive to manufacture via traditional casting and machining methods. Low density lattice structures for lightweight construction are one such example. However, there currently are no well-developed guidelines for designing and reliably manufacturing these structures. Literature on the topic is fragmented and usually only covers a limited aspect of the complex relations between process parameters, microstructure, lattice geometry and mechanical properties. This work covers the edge case of small diameter struts manufactured from AlSi10Mg via Laser Powder Bed Fusion (L-PBF) using the single contour exposure strategy, which is necessary to ensure sufficient geometric accuracy. Various cubic strut-based lattice geometries are manufactured using four laser parameter combinations corresponding to different area energy densities and beam offsets. The influence of process parameters and heat treatment on the microstructure and mechanical properties is investigated. Results show that the microstructure of filigree lattice struts can be tailored by the selection of process parameters, resulting in either uniform or core–shell structures depending on the laser power, while the macroscopic mechanical properties are mainly determined by the lattice geometry and relative density.

* Corresponding author.
  E-mail address: marcel.sos@tu-darmstadt.de (M. Sos).

1. Introduction

The manufacturing industry strives for an optimum between sustainability, cost and resource efficiency. In this context, additive manufacturing has established itself as a disruptive technology by offering constructive flexibility and a significant degree of weight reduction [1,2]. In addition to the increased lightweight potential they offer, architected cellular structures, such as honeycombs or lattices, can drastically reduce the printing time and therefore make additive manufacturing more viable in terms of time-to-market, improving competitiveness [3–5]. Due to the possibility of tailoring properties through their geometrical configuration, interest in these structures for dynamic and energy absorption applications is growing [6–8].

However, despite the possible reductions of weight and resource consumption, the efforts required for both manufacturing and post-processing prevent this technology from being a competitive contender against conventional manufacturing processes in most cases. As a matter of fact, additive manufacturing is often employed for rapid prototyping or complex applications with small batch size while its use in serial production is rather limited [9,10]. The main challenge lies in understanding and predicting the mechanical performance of additively manufactured parts. Despite extensive research for more than a decade, the literature on the relationships between process parameters, microstructures and mechanical properties of additively manufactured bulk materials is still fragmented, yet, it offers promising insights on controllable process induced properties [11–15], with defects playing a major role [6,16]. Latest research is attempting to establish a clear relationship for the interactions between process parameters and mechanical properties, including lattice structures [17–20]. It has been shown for different materials that the mechanical performance of lattice structures is intrinsically linked with their structural integrity, their geometrical deviations with respect to the initial design and the employed printing parameters [21–27]. However, there are not just the common defects (e.g., geometrical inaccuracy, porosity or surface roughness) and common correlations between printing parameters and resulting microstructures known from bulk samples that need to be considered. The microstructure of lattice materials is also affected by their geometrical configuration. Local texturing due to miniaturization effects caused by changes in the dimensionality of the heat flow can play a non-negligible role at the sub-millimeter scale, thus, affecting mechanical properties [28–34]. Current research is therefore addressing the question of the right scanning strategy and design guidelines for small scale features [35–41]. Out of many available strategies, contour exposure delivers the highest quality in terms of surface roughness and geometrical accuracy at the submillimeter scale [19,37,42,43] and seems to be the most suitable approach for the manufacturing of thin-walled lattices. In the available literature, strut diameters in the range of 500 to 1000 µm are typically used and manufactured using hatch or a combination of hatch and contour exposure [21,26,28,31,32,44,45].

Against this backdrop, the aim of this study is to provide an insight into the influence of process parameters on the microstructure and mechanical properties of AlSi10Mg lattice structures in order to understand and enable their potential for lightweight applications. This contribution focuses on the relationship between manufacturing parameters and part properties for the case of low strut diameters in the range of 270 to 370 µm manufactured with single contour exposure, as well as the influence of the contour overlap as an additional design parameter. This not only covers different line energies, but also different geometries, both, on the local scale by changing the strut diameter as well as on the macro scale by using different lattice unit cells. The local manufacturing induced properties are assessed in terms of microstructure and hardness and compared with the global deformation behaviour and macroscopic mechanical properties. Since AlSi10Mg structures are typically heat treated after L-PBF, the characterisation covers not only as-built but also subsequently annealed conditions. Based on the obtained results, the impact of local properties and global structural parameters (lattice type and relative density) on the mechanical performance of lattice structures is evaluated.

2. Experimental methodology

2.1. Sample design and manufacturing

Lattice samples were designed with face centered cubic (f2cc as well as f2ccz featuring vertical struts aligned with the build direction) and body centered cubic (bcc) unit cells. Modified unit cell designs seen in Fig. 1 were chosen to avoid the issues of semi-cylindrical and unjoined struts at the outer sample edges. The f2ccz geometry was used because of its good specific properties [21,46], with the f2cc and bcc structures serving as a comparison with no z-aligned struts and different strut inclination angles (α = 45° for f2cc(z) and 35.26° for bcc). The CAD models had a cross-section of 5x5 and a height of 7 unit cells with a strut diameter of 100 µm and a cell size of 3.25 mm.

Samples were manufactured using an EOS M 290 L-PBF machine under Argon inert gas atmosphere with a laser focus diameter of 80 µm, a layer thickness of 30 µm and a build plate temperature of 125 °C, employing the single contour exposure strategy. The powder composition provided by EOS can be found in Table 1 [48].

The parameter combinations used for sample manufacturing are listed in Table 2. The combinations of laser power and scan speed, as well as the beam offsets necessary to achieve the targeted overlap values were chosen for their good manufacturability and geometric accuracy. The parameters are based on previous work by Großmann et al., in which melt pool dimensions and the process parameter window for single contour exposure were investigated [19,49].

Fig. 2 shows a schematic of the contour exposure strategy. An offset of Δt_c from the model outline t_{CAD} results in the laser path diameter d_h. (right) shows the resulting strut diameter t, which depends on the melt pool width b and the amount of overlap.

2.2. Sample preparation and testing

Samples were heat treated in air for 2 h at 300 °C, 350 °C, 400 °C, 450 °C and 500 °C, followed by water quenching, with the 400–500 °C treatments only being applied to 300_30 samples. The heat treatment temperatures and time were selected in line with available literature on direct aging (DA) of additively manufactured AlSi10Mg [51–54]. For microstructural characterization the samples were hot mounted, ground and polished to 0.25 µm diamond suspension, followed by fine polishing and vibropolishing with Colloidal Silica suspension. Contrasting for microscopy was done by etching with Keller's reagent (1 % HF) for approximately 25 s.

SEM imaging was carried out using a TESCAN MIRA3 SEM with an acceleration voltage of 15 kV, equipped with an EDAX DigiView EBSD system. EBSD measurements were performed with a step size of 500 nm. Neighbour Pattern Averaging & Reindexing (NPAR), in which each pattern is averaged with its nearest neighbours and then reindexed [55], as well as grain CI standardization, were used for dataset cleanup and points with a confidence index below 0.1 were ignored.
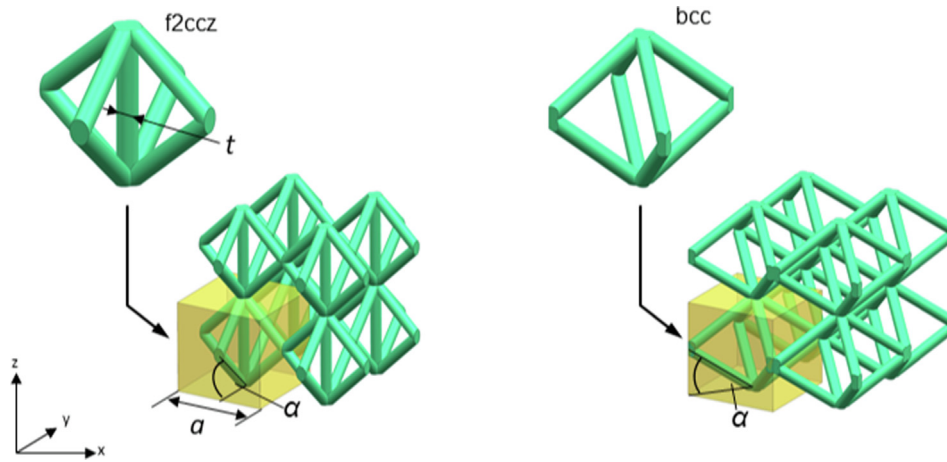
Fig. 1. Used unit cell geometries for f2cc(z) (left) and bcc (right) samples with the cell size *a*, strut diameter *t* and inclination angle α. Adapted from [47]

Table 1
Alloy composition of the used AlSi10Mg powder.

Element	Al	Si	Fe	Cu	Mn	Mg	Ni	Zn	Pb	Sn	Ti
wt.%	Bal.	9–11	<0.55	<0.05	<0.45	0.25–0.45	<0.05	<0.10	<0.05	<0.05	<0.15

Table 2
Parameter combinations used for sample manufacturing and the resulting diameter of vertical struts. Note that the strut diameter is not a primary design parameter in this work, but results from the targeted overlap percentage.

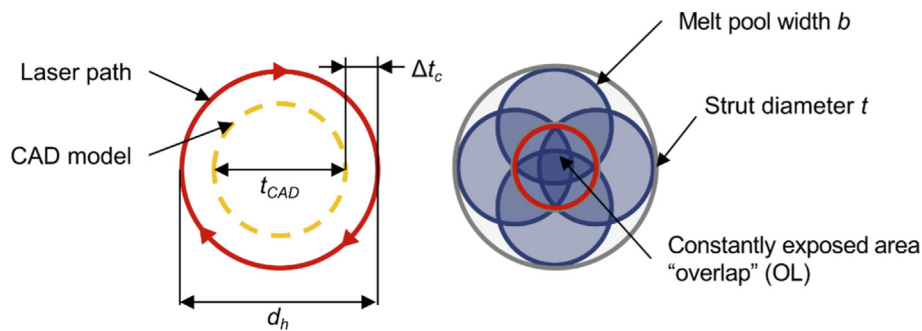| Parameter #	P [W]	V [mm/s]	OL [%]	Contour Offset [μm]	Strut Diameter [μm]
200_30	200	2500	30	3.45	286 ± 8
200_50	200	2500	50	16.75	268 ± 7
300_30	300	2500	30	−7.75	372 ± 7
300_50	300	2500	50	8.75	363 ± 6

Fig. 2. Illustration of the single contour exposure strategy used in this work, adapted from [50]. A comparable concept has been shown by Vrána et al. [43].

Compression tests were done with an Instron 5967 universal testing machine equipped with a 30 kN load cell at an initial strain rate of 10^{-3} to a maximum displacement of 10 mm. Strain was measured using the crosshead position. Relative densities for the normalization of test results were calculated using the weight of the samples *m*, the nominal dimensions of the CAD models, resulting in the volume *V* and the bulk density ρ_{bulk}. Normalized stress values were obtained by dividing the engineering stress σ by the average relative density ρ_S: $\sigma_{norm} = \frac{\sigma}{\rho_S}$ (1) with $\rho_S = \frac{m}{V}/\rho_{bulk}$ (2), assuming a bulk density of 2.67 g/cm^3 [48]. Details about the relative density measurements can be found in the appendix.

Porosity was neglected because lattice samples manufactured in the selected parameter space are greater than 99 % dense according to Archimedean density measurements conducted on f2ccz samples by Großmann et al. [19]. The same L-PBF system, CAD model and exposure strategy were used in this work. This makes the influence of porosity small compared to changes in the strut diameter.

Indentation tests were performed using a Keysight G200 nanoindenter equipped with a Berkovich tip and a CSM (Continuous Stiffness Measurement) module. A maximum displacement of 1300 nm and a maximum force of 50 mN were set as stopping

criteria. Hardness values were averaged from indentation depths above 500 nm.

3. Results

3.1. Microstructural properties

Fig. 3 shows EBSD IPF maps of vertical struts of lattice samples 200_30 (left) and 300_30 (right). The 200_30 strut displays a [1 0 0] texture parallel to the build direction while 300_30, which has been manufactured with higher laser power, shows distinct outer and inner zones with the latter having [1 1 0] and [1 1 1] texture components parallel to the build direction. Strut 200_30 has a homogeneous α-Al grain size of 23.69 ± 13.06 μm, which is similar to the outer region of strut 300_30, which has a grain size of 26.65 ± 17.98 μm. However, the inner region of strut 300_30 exhibits a finer grain size of 10.21 ± 4.98 μm.

These local microstructural differences also affect the precipitated Si, both on the as built and heat treated states, as can be seen for etched 200_30 and 300_30 samples in Fig. 4. The as built state of sample 200_30 can be seen in (a) and (c). During solidification, a continuous network is formed by silicon which precipitates from the melt after the formation of primary α-Al [30,56,57]. The spacing of the silicon cells observed in the as built state is mostly uniform throughout the cross-section apart from some localized coarser streaks. Sample 300_30 (b,d) exhibits distinct outer and inner regions with significant differences in silicon spacing, which becomes finer towards the center of the strut. The measured spacing is given in Table 3. The given values are the averages obtained from 3 struts. The significant amount of porosity visible in the cross-section in Fig. 4 is caused by the etching process during sample preparation and not representative of the sample in its pristine state.

After the 300 °C heat treatment the original shape of the silicon cells is still visible in sample 200_30 (Fig. 4 e), but the connectivity of the network has been significantly reduced. The outer area of sample 300_30 shows the same trend. However, in the inner area (f) the structure has fragmented completely and the precipitated silicon agglomerated into particles with sizes ranging from approximately 100 to 400 nm.

A similar structure is found in strut 200_30 after the 350 °C heat treatment (g). The silicon network structure is no longer visible

and particle sizes range from 140 to 600 nm. The inner area of strut 300_30 (f) shows a different, bimodal particle size distribution featuring small (approx. 100 nm) and large (approx. 800 nm) particles.

3.2. Local mechanical properties

Fig. 5 shows the hardness maps obtained via nanoindentation of struts from 200_30 (left) and 300_30 (right) lattice samples in the as built (top), as well as 300 °C (middle) and 350 °C (bottom) heat treated states.

In the as built state, strut 200_30 shows a mostly uniform distribution of hardness in its cross-section (1.67 ± 0.1 GPa). The higher microhardness values of up to 2–2.5 GPa reported in literature for the as built state [52,58] can be attributed to the indentation size effect, which causes higher hardness to be measured at low indentation depths [59], leading to overestimations.

Strut 300_30 has distinct areas of lower (1.4–1.5 GPa) and higher (up to 1.99 GPa) hardness corresponding to areas of coarser and finer silicon spacing. Between the outer and inner areas, which feature the lowest and highest hardness respectively, a transition zone with hardness comparable to that of strut 200_30 can be found.

The same trends can be observed after heat treatment (Fig. 5 b, c). The average hardness decreases with an increase in heat treatment temperature. For both the 300 °C and 350 °C states, the struts manufactured using parameter set 200_30 show a uniform hardness of 1.19 ± 0.02 GPa and 0.97 ± 0.02 GPa respectively, while areas of lower and higher hardness can still be seen for the 300_30 samples despite the fragmentation of the silicon network. These differences could potentially be attributed to differences in silicon particle spacing.

3.3. Macroscopic mechanical properties

Fig. 6 shows the density normalized stress–strain-curves of compression tests of f2ccz 200_30 and 300_30 lattice samples in the as built and various heat treated states. In the following, a single representative curve is shown for each sample state. A comparison of several lattice samples manufactured with the same parameter set, as well as a statement about deviations and the representativity of the results, can be found in the appendix. The
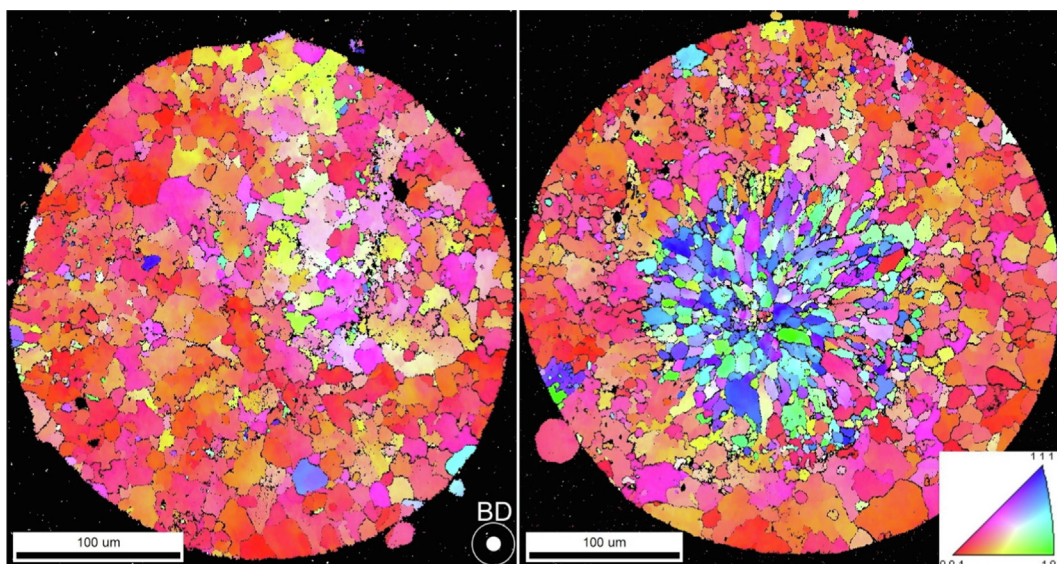

Fig. 3. EBSD maps of vertical struts from f2ccz lattice samples manufactured with a laser power of 200 W (left) and 300 W (right), both with an overlap of 30 %. The build direction (BD) is perpendicular to the image plane.
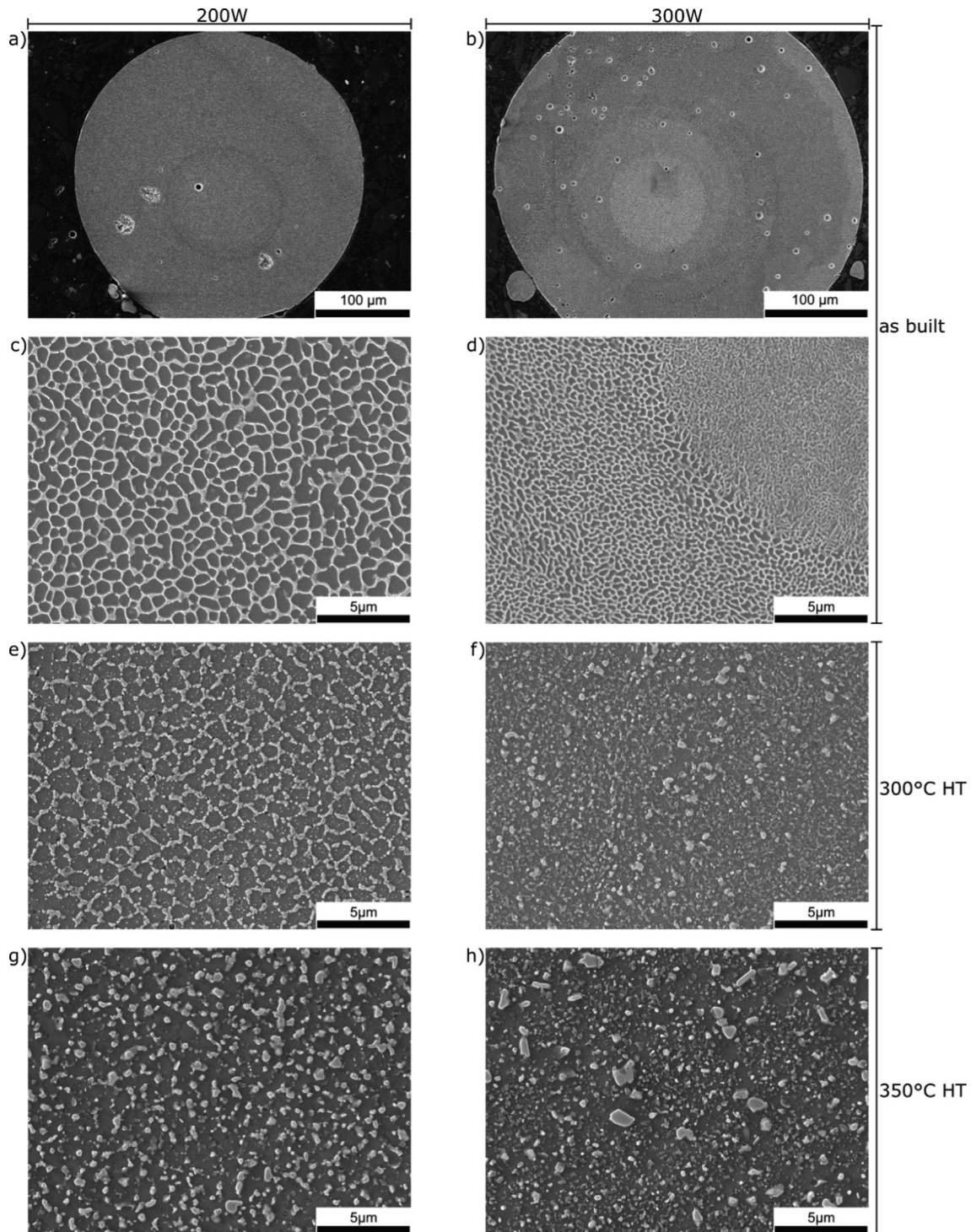
Fig. 4. SEM images of the etched microstructure of 30 % overlap vertical struts manufactured with a laser power of 200 W (left) and 300 W (right) in the as built state (a-d) and after the 300 °C (e,f) and 350 °C (g,h) heat treatment.

Table 3
Spacing of precipitated silicon in the as built state. The core spacing for sample 300_50 is likely overestimated due to etching damage to the microstructure.

Sample	Si spacing (shell) [nm]	Si spacing (core) [nm]
200_30	685 ± 51	658 ± 63
200_50	682 ± 48	704 ± 42
300_30	803 ± 94	203 ± 17
300_50	849 ± 49	261 ± 17

200_30 sample in the as built state shows a peak stress of 50 MPa at a strain of approximately 4 %, followed by a drop to 1.3 MPa. The initial peak is followed by several smaller ones as the strain increases, each with a significant stress drop. The 300 °C heat treated sample also shows a peak at 4 % strain, but the strength of the lattice is reduced to 43 MPa. Subsequent peaks still appear, but the magnitude of the accompanying stress drop is reduced. In the 350 °C heat treated state an initial peak of 34 MPa can be seen, followed by a plateau fluctuating around approximately 25 MPa.
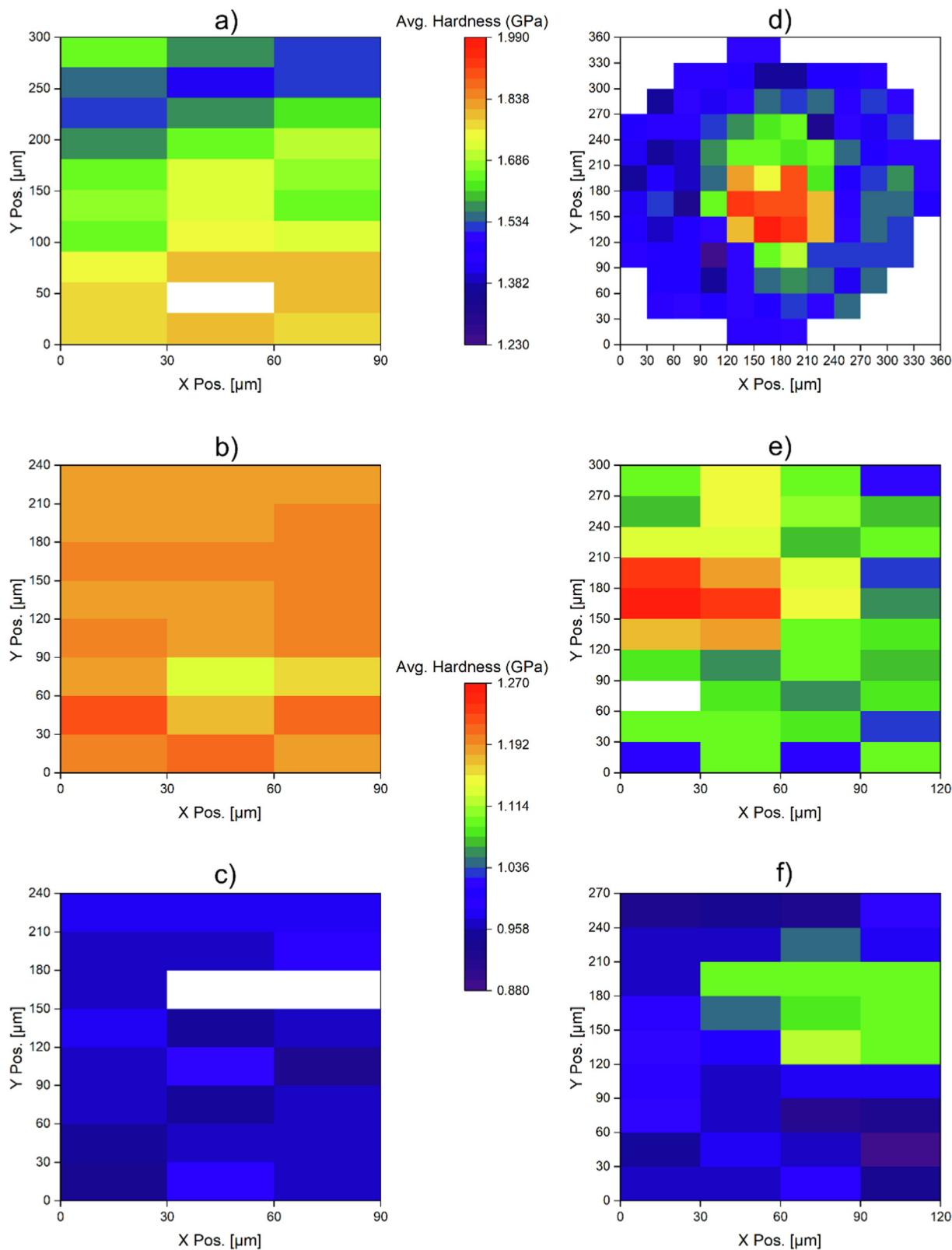
Fig. 5. Nanoindentation hardness maps of vertical struts manufactured at 200 W (a-c) and 300 W (d-f) laser power in the as built (a,d), as well as 300 °C (b,e) and 350 °C (c,f) heat treated states. Note the different scale bars for as built and heat treated samples. Indent arrays positioned approximately around the center of each strut, except (d) which encompasses the entire cross-section.

Similar behaviour is observed for the 300_30 sample. In the as built state, the initial peak of 73 MPa at 4 % strain is followed by a drop to 2.6 MPa and subsequent smaller peaks. The 300 °C heat treatment causes a reduction of the specific strength and moves the curve closer to a constant plateau. The 350 °C and 500 °C heat treated samples behave similarly. An initial peak can still be seen,
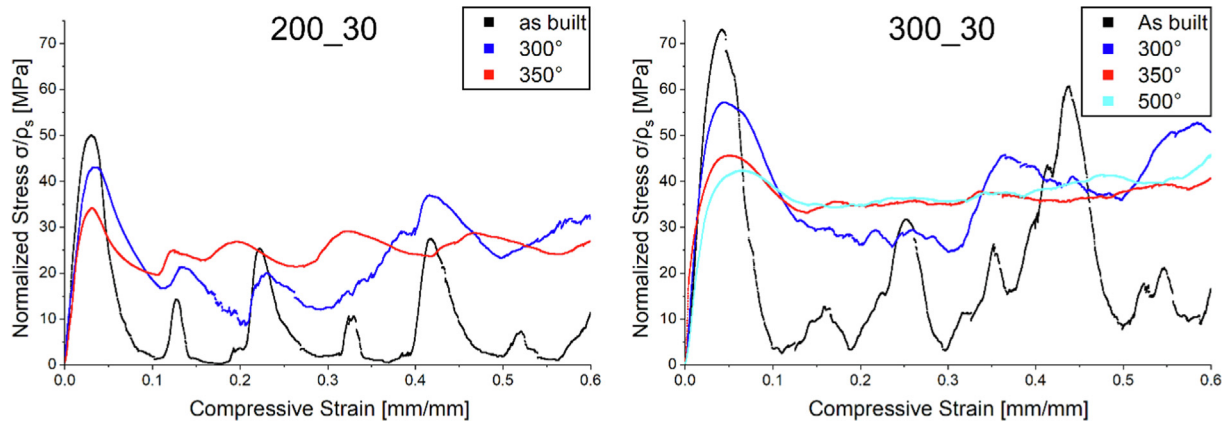
Fig. 6. Stress–strain curves of f2ccz lattice samples manufactured with 30 % overlap and laser powers of 200 W (left) and 300 W (right) in the as built and heat treated states.

but it is followed by a plateau region with minor stress fluctuations. The plateau stress is approximately 35 MPa for both samples. The 400 and 450 °C heat treated samples are omitted from the figure for better readability and showed a comparable plateau stress. Densification does not set in, indicating that strains greater than 0.6 are required for opposing unit cell walls to impinge.

It can be seen that the effect of heat treatments on the samples is the same regardless of the microstructural differences seen in Fig. 4. During heat treatment the silicon network is fragmented, which leads to lower strength, increased ductility and a transition from brittle to ductile deformation behaviour of the lattice.

A comparison of the deformation behaviour of the different lattice geometries manufactured with parameter set 300_30 after heat treatment is shown in Fig. 7 via density normalized stress–

strain-curves and pictures of lattice samples taken at different strains. The as built state is omitted because its brittleness makes it unsuitable for practical applications, but the data can be found in the appendix.

After the 300 °C heat treatment both the f2ccz and f2cc sample exhibit a series of peaks corresponding to the formation of diagonal shear bands, in which deformation is localized. Stress drops after each peak are less pronounced for the f2cc structure. Failure of unit cells in the shear band occurs via the bending of struts in close proximity to the nodes. In the case of f2ccz, the buckling of vertical struts leads to the loss of strength after the initial peak. It can be seen that at high strains the unit cells outside of the shear bands also deform. Shear band formation is not observed in the bcc lattice. Instead, it displays a constant stress plateau and deforms sim-
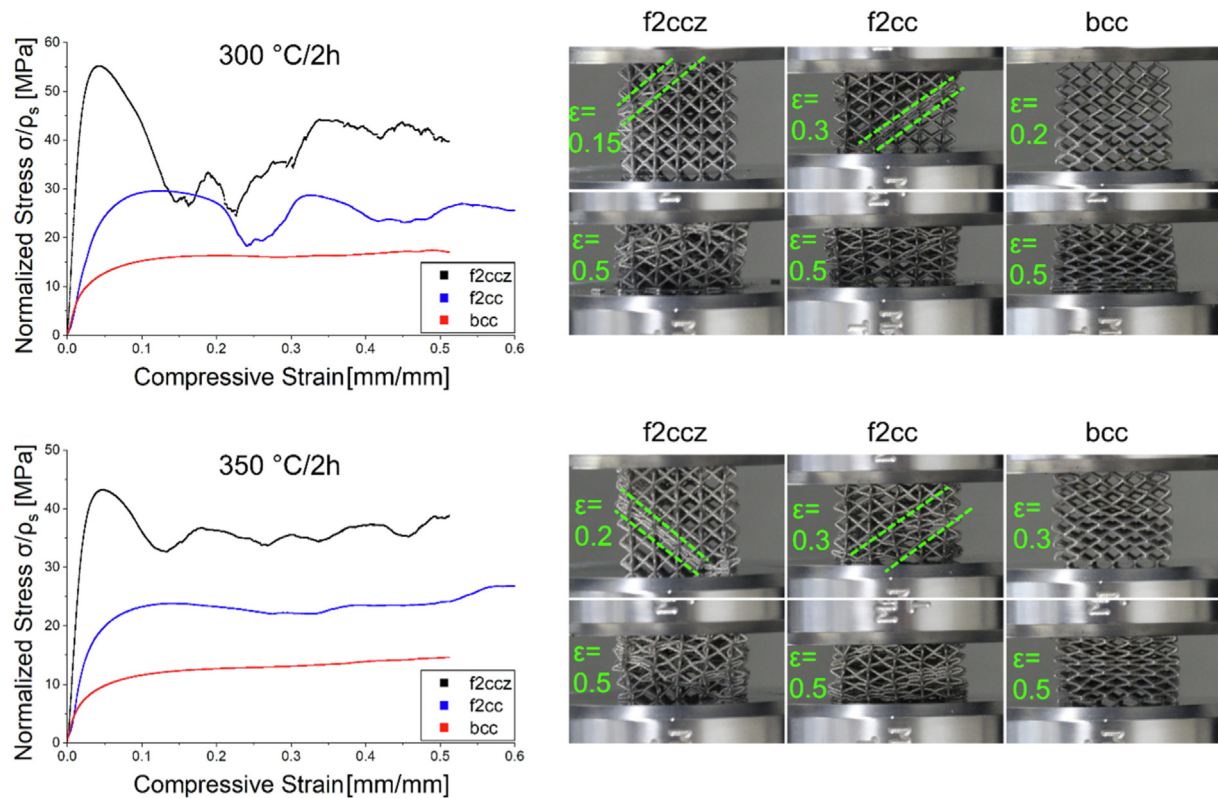

Fig. 7. Normalized stress–strain-curves and images of lattice samples manufactured with 30 % overlap and 300 W laser power after 300 °C (top) and 350 °C (bottom) heat treatment.

ilarly to the layer-by-layer mode expected for density graded structures [44,45]. This gradient in deformation could be caused by differences in friction at the top and bottom surface of the sample as a result of preparation.

The 350 °C heat treatment causes a reduction of specific strength for all samples. Shear band formation can still be observed in the f2ccz and f2cc sample, but both curves are closer to a constant stress plateau due to the absence of brittle strut failure. Barrelling is visible in the bcc sample and it deforms uniformly at high strains.

Fig. 8 shows the influence of overlap and laser power on the specific stress–strain curves of bcc samples after the 350 °C heat treatment. An increase in laser power, and consequently strut diameter, results in a higher plateau stress. It is possible that a variation in overlap has an effect on mechanical properties. However, the differences between the samples manufactured with an overlap of 30 % and 50 % are within the range of variation expected as a result of the position of the sample on the build plate, which can cause deviations of up to 18 % due to local differences in inert gas flow [19]. The parameter comparison of f2ccz and f2cc samples can be found in the appendix.

4. Discussion

4.1. Microstructural influence of process parameters

The present results clearly demonstrate a marked effect of processing parameters on the local microstructures of vertical struts in f2ccz lattices. Considering that microstructural features such as grain orientation, grain size or particle spacing act as a fingerprint for the direction of heat flow and cooling speed, they can provide insights into the impact of processing parameters on the local conditions during the additive manufacturing process.

Vertical struts manufactured with a laser power of 200 W exhibit a [1 0 0]-texture in build direction along with a uniform grain size and spacing of precipitated silicon. Consequently, the heat flow and cooling rates seem to be nearly constant throughout the entire cross-section. With [1 0 0] being the preferred solidification direction along thermal gradients for Aluminium and other fcc metals [14,56,60–62], it is evident that the whole strut solidifies along the build direction. This can be attributed to miniaturization effects, which means that the melt pool diameter is no longer insignificantly small with respect to the strut diameter but rather approaching similar dimensions. Given that the dissipated heat via the surrounding powder bed is marginal compared to the one

via the solid strut [33,63], the heat flow becomes uniaxial pointing downwards into previously manufactured layers. In literature, the transition point for miniaturization effects is typically in the range of one to several millimetres for microstructural and mechanical properties respectively [33,63–65], so they apply for all tested samples.

However, an increase of the laser power from 200 W to 300 W alongside with an increase in diameter by approx. 30% is still well within the realm affected by miniaturization, yet it no longer creates a homogenous cross-section but leads to a core–shell-structure. The outer region still shows a similar microstructure as with 200 W, the central section deviates from the [1 0 0] fibre texture and features mostly [1 1 0] and [1 1 1] components parallel to the build direction as well as a smaller grain size and finer silicon spacing. This implies that the heat flow in the central area of the larger struts is no longer parallel to the build direction but also contains a radial component. Similar behaviour is known from overlapping areas between melt tracks of bulk material [11] and in struts manufactured via multi-contour exposure [37].

In addition, there are also differences in solidification speed, evidenced by the sizes of α-Al grains and the spacing of precipitated silicon. Grain size and dendrite spacing are inversely proportional to the cooling rate, indicating that the inner area of a large diameter strut solidifies faster than the outer area. The influence of cooling rate on silicon spacing can also be observed in bulk material, in which melt pools display distinct zones with different spacing as a result of local differences in cooling rate [54,66–69]. According to Tang et al., the cooling rate can be estimated via the following relationship [70]: $\lambda = 43.2\dot{T}^{-0.324}$ (3), in which λ is the Silicon cell size and $\dot{T}$ the cooling rate in K/s. Using the silicon spacing from Table 3, the resulting cooling rates are approximately 3.6×10^5 K/s for struts manufactured with a laser power of 200 W, 2×10^5 K/s in the outer area and 1×10^7 K/s in the inner area of struts manufactured with a laser power of 300 W. These values are in line with literature, where cooling rates in the order of magnitude of 10^3 up to 10^6 are typically reported [54,66,71]. Additionally, Narra et al. simulated a cooling rate of approximately 1×10^7 K/s for a laser parameter combination resulting in a silicon cell size of 200 nm [72].

Based on the microstructural observations, a hypothetical solidification scenario for high laser power is shown in Fig. 9. High energy input in the central area, which is constantly exposed due to the contour overlap, leads to overheating effects, which cause it to remain liquid while the outer area can already solidify. The central area then solidifies after the contour pass is completed with heat flowing downwards and outwards, enabling faster thermal transfer as well as resulting in a different texture due to the different solidification direction.

Utilizing modern process monitoring techniques, many of which are outlined in a recent review by AbouelNour and Gupta [73], the melt pool development as a function of area energy input could potentially be observed during manufacturing, allowing a direct validation of the mechanisms proposed here. Additionally, the grain sizes and silicon spacing observed in this work, could serve as a calibration or validation for the calculation of local cooling rates and thermal gradients in process simulations, thus helping to improve their predictive capabilities and shortening product development cycles.

The microstructural changes during heat treatment are in line with previous results reported in literature. Heat treatment at 300 °C results in a perceived blurring of melt pool boundaries due to the reduced connectivity of the silicon network, but the remains of the original structure remain visible until the temperature is increased above 320 °C [51,74]. Snopiński et al. heat treated additively manufactured AlSi10Mg at 300 °C for 8 min and
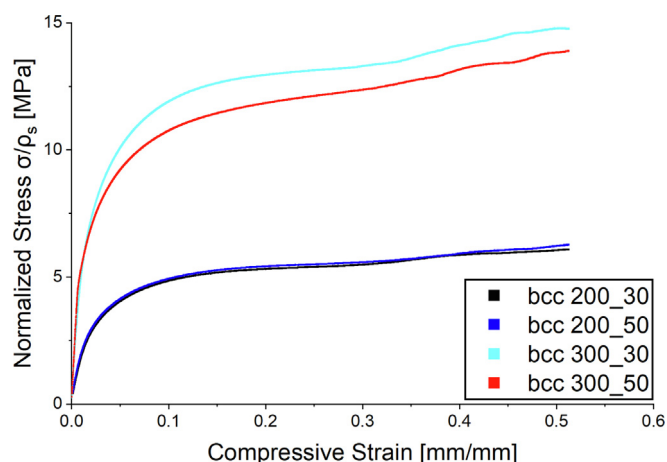

Fig. 8. Normalized stress–strain curves of bcc lattice samples manufactured with 200 W and 300 W laser power and overlaps of 30 % and 50 %.
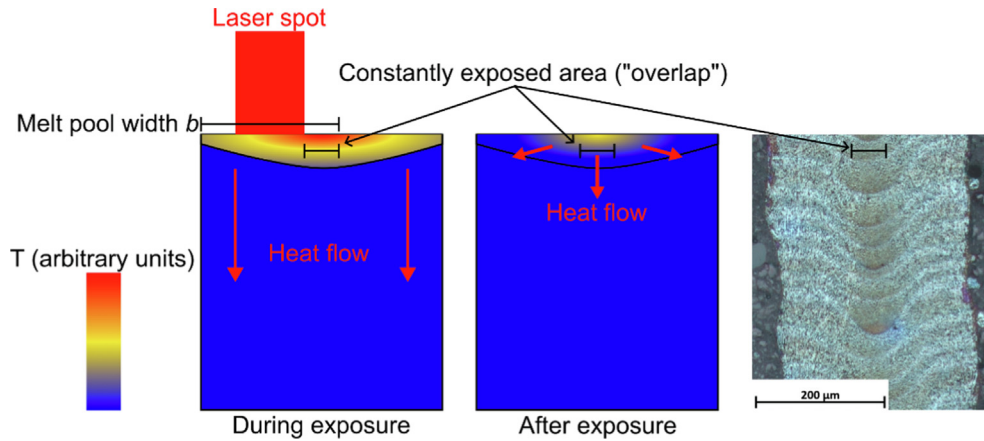
Fig. 9. Illustration of the hypothesized local overheating and solidification mechanism at high laser power showing the laser beam and heat transfer during solidification. On the right, the cross-section of a vertical strut is shown.

observed a similar microstructural change [75,76], indicating that heat treatment times in the order of magnitude of several hours might not be necessary. A contiguity parameter could be beneficial in describing the microstructural transition occurring during the 300 °C heat treatment. However, that requires resolving not only Al-Si phase boundaries but also Si-Si grain boundaries [77], which was not achieved in this work.

In the central areas of large diameter struts the original structure is already no longer visible after the 300 °C heat treatment. Assuming an equal volume fraction of precipitated silicon throughout the cross-section, the much finer spacing in those regions would result in an increased surface area, which could make the particles thermodynamically less stable.

The differences in microhardness across struts and heat treated states are a result of several factors. In the as built state, the silicon network is almost two orders of magnitude finer than the α-Al grain size, which makes it the main factor in inhabiting dislocation movement. Takata et al. reported low angle boundary substructures along the silicon particles [30,56] and due to the high cooling rate the Al matrix is supersaturated with silicon, causing some solid solution strengthening [30,59,78]. The highest hardness in the as built state is therefore measured in the centre of large diameter struts, which feature the finest distribution of silicon. Consequently, the uniform hardness measured throughout the cross-section of low diameter struts mirrors the uniform distribution of silicon.

Hardness decreases with heat treatment due to the fragmentation of the silicon network and further coarsening of particles upon an increase in temperature from 300 to 350 °C. Additional silicon precipitates from the matrix [67,74,78], which reduces the effect of solid solution strengthening and recovery may take place, reducing the dislocation density. The local differences in hardness of large diameter struts after heat treatment could be caused by differences in the spacing and volume fraction of particles.

These results show that within the realm of miniaturization effects it is still possible to influence the microstructure of small-scale lattices via the variation of process parameters, producing either homogeneous or graded structures.

4.2. Mechanical properties

In the as built state, all tested samples exhibit brittle behaviour and failure via shear localization, showing that below a certain level of ductility in the AlSi10Mg material, the lattice type does not affect the failure mode. Differences emerge after ductilization via heat treatment. The formation of shear bands during compres-

sion is only observed for f2ccz and f2cc lattice samples while bcc samples deformed uniformly.

The comparison of different heat treatment states reveals that past a certain point of microstructural change there are no significant differences in mechanical properties of the lattice, evidenced by the 350 to 500 °C heat treated states having the same plateau stress, despite differences in the properties of bulk material [67].

The f2ccz and f2cc lattice samples show localized deformation via diagonal shear bands, which have been commonly observed for Aluminium alloy lattices [17,44,45,53], as well as lattices manufactured from other materials [79–83] and sheet-based structures like triply periodic minimal surfaces (TPMS) or honeycombs [84–87]. It has been shown that the formation of shear bands depends on the unit cell geometry [80,86], shape of the struts [88] and heat treatment [53]. The mechanical properties of lattices in general depend on the properties of individual struts [89] with lower strut aspect ratios, and consequently higher relative densities of the lattice, resulting in higher resistance to buckling. A similar relationship has also been highlighted in a recent study by Banait et al. [90], in which the deformation behaviour of IN718 lattice structures changed after a precipitation hardening heat treatment, attributed to the decreased buckling strength of struts. This shows that the failure mode of lattices could possibly be switched
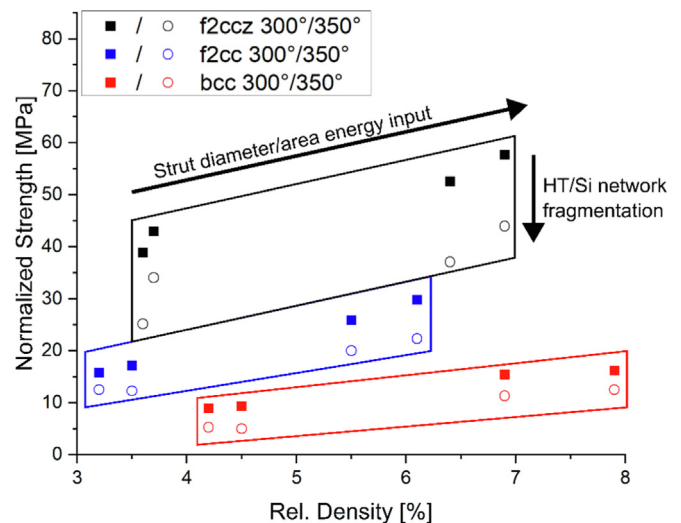

Fig. 10. Normalized compressive strength of the tested lattice geometries after heat treatment as a function of relative density.

between brittle and ductile depending on certain breakpoints in the properties of the constituent material, which can be adjusted via heat treatment.

Looking at the normalized strength of the heat-treated lattice samples as a function of relative density (Fig. 10), the role of the lattice geometry on the macroscopic mechanical properties is apparent. It can be seen that, for a given relative density, the f2ccz lattice has the highest specific strength, which is caused by the vertical struts aligned with the loading direction. It is followed by f2cc, with bcc showing the lowest specific strength. This order of relative performance of the different lattice geometries is in line with other literature data [21,46]. All tested lattice geometries show a linear increase in specific strength with increasing strut diameter and relative density, which can be attributed to the differences in strut aspect ratio and potentially the decreasing influence of surface roughness effects. The same trend of a linear increase of specific properties has been reported for lattices manufactured from 316L stainless steel over a wider range of relative densities [80]. In the work of Suzuki et al. [53] a normalized strength of approximately 30.5 MPa was reported for a bcc lattice with a relative density of 16.4 % after heat treatment for 2 h at 300 °C. This value is outside the scope of relative densities tested here, but follows the same trend.

The trapezoid areas in Fig. 10 corresponding to the different lattice types clearly indicate that the unit cell geometry is the main factor governing the quasi-static mechanical performance of lattices once a sufficient level of ductility has been reached via heat treatment. Despite their microstructural differences, samples manufactured using low and high laser power behave similarly, as the same deformation behaviour was observed independent of the strut diameter and the presence or absence of a core–shell-structure, as seen in Fig. 6. One reason for this could be the similarity of microstructures for low and high laser power in the outer region of the struts that is more relevant for the mechanical performance under bending loads than the core region, given that highest stresses and crack initiation sites are located at the surfaces of struts [53,88]. Therefore, the silicon spacing in the central region of a strut has little to no influence on its mechanical properties.

Further work is required to understand the exact causes of shear localization in cellular materials and to correlate local mechanical properties of single struts, both under tensile and bending loads, with those of the lattice and the influences of unit cell type and relative density. The influence of the overlap parameter should also be further investigated while keeping other possible factors that are known to influence part properties in mind.

While the observed microstructural differences in this work did not influence the quasi-static mechanical behaviour of lattice structures, it is possible that the core–shell-gradient produced by the higher laser power impacts fatigue performance, warranting future research. Additionally, the differences in texture are expected to have a stronger effect on materials that show elastic anisotropy, such as nickel, copper or austenitic steels, and could serve to further tailor the properties of additively manufactured small-scale structures.

5. Conclusion and outlook

In this work, the microstructural influence of laser power and beam offset on thin-walled AlSi10Mg lattice structures manufactured via single contour exposure L-PBF was investigated via EBSD, SEM imaging and nanoindentation and different solidification mechanisms for low and high area energy input were proposed. Compression tests were carried out on heat treated f2ccz, f2cc and bcc lattice samples manufactured with the same parameter

combinations and their mechanical properties were characterized. The main results of this study are the following:

(1) Different process parameters result in significant differences in the microstructures of vertical struts. At a laser power of 200 W a uniform [100]-texture in build direction is observed, while an increase in laser power to 300 W leads to the emergence of a core–shell-structure with the central region showing [110] and [111] texture components.

(2) The inner and outer regions feature different spacings of precipitated silicon with the central, differently textured, region showing significantly finer structures. Both of these effects have been attributed to local overheating during manufacturing.

(3) Heat treatment at 300 °C for 2 h results in fragmentation of the silicon network and a decrease in hardness. After heat treatment at 350 °C for 2 h, the shape of the original precipitation structure is no longer visible and hardness is further reduced.

(4) After both heat treatments, the formation of macroscopic shear bands is observed in f2ccz and f2cc samples while bcc samples deform uniformly.

(5) Lattice samples manufactured with different process parameter sets exhibit the same deformation behaviour, regardless of their differences in microstructure and local mechanical properties. The observed trends indicate that the quasi-static mechanical response of lattices is primarily governed by the unit cell type and relative density, which is in turn influenced by the process parameters.

CRediT authorship contribution statement

Marcel Sos: Validation, Investigation, Writing – original draft, Writing – review & editing, Visualization. **Guillaume Meyer:** Conceptualization, Resources, Writing – original draft, Writing – review & editing, Visualization, Supervision. **Karsten Durst:** Writing – review & editing, Project administration. **Christian Mittelstedt:** Resources, Writing – review & editing, Project administration. **Enrico Bruder:** Conceptualization, Writing – review & editing, Supervision.

Data availability

Data will be made available on request.

Declaration of Competing Interest

The authors declare that they have no known competing financial interests or personal relationships that could have appeared to influence the work reported in this paper.

Acknowledgements

Appendix

Microstructural properties

Fig. 11 shows SEM images of etched vertical struts manufactured with parameter sets 200_50 and 300_50 in the as built and heat treated states. In the as built state the inner section of the 300_50 struts has been damaged by the etching process (d),
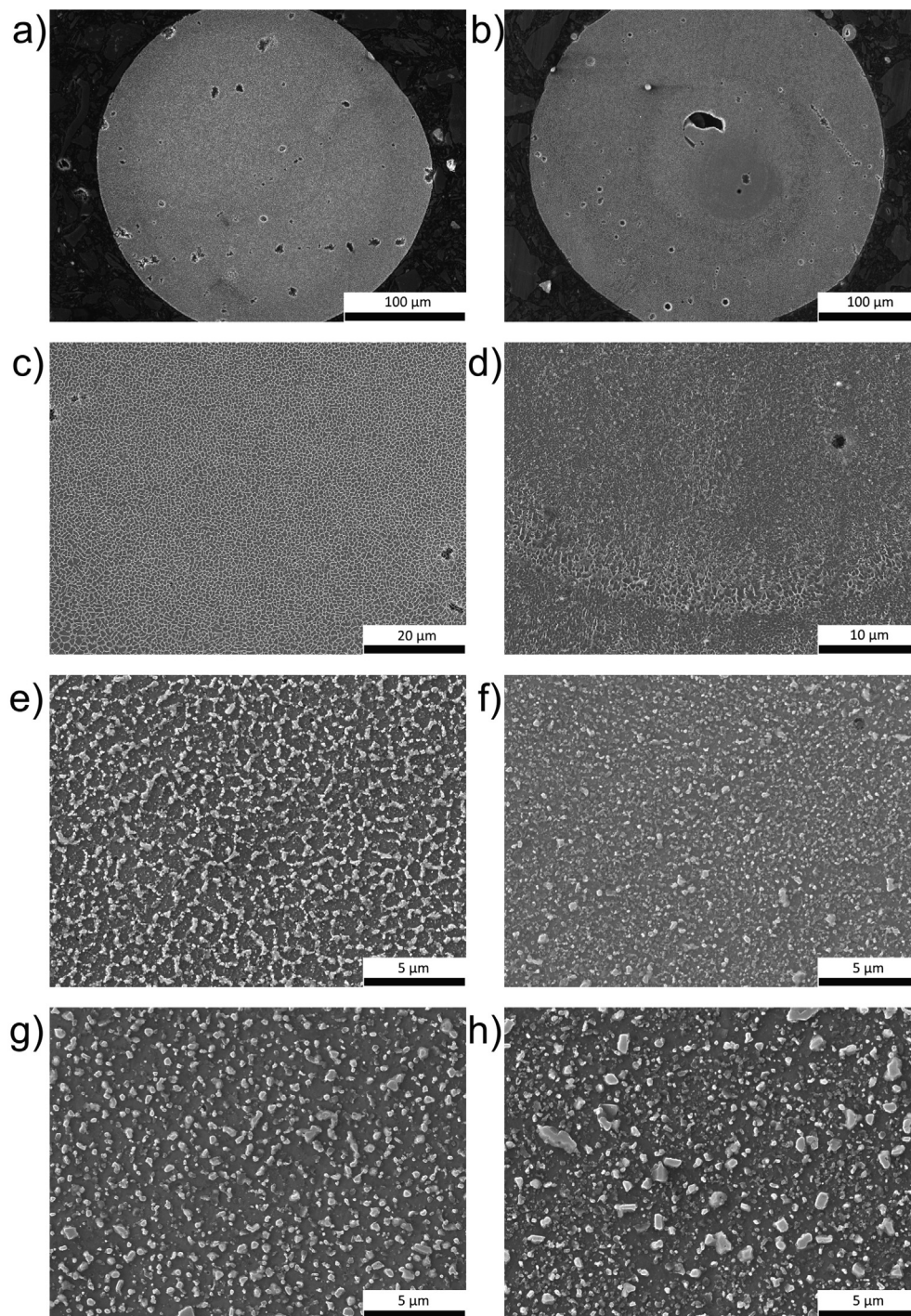
Fig. 11. SEM images of the etched microstructure of 50 % overlap vertical struts manufactured with a laser power of 200 W (left) and 300 W (right) in the as built state (a-d) and after the 300 °C (e,f) and 350 °C (g,h) heat treatment.

which makes an overestimation of the silicon spacing compared to parameter set 300_30 likely. The porosity visible in the cross-section can be attributed to damage caused by the etching process. The cross-section of a 300_30 strut that has been ground and polished again after etching is shown in Fig. 12 for comparison.

Fig. 13 shows a light microscopy image of the cross-section of an etched vertical strut manufactured with a laser power of 250 W and an overlap of 34.7 %. The melt tracks corresponding to the individual layers can be seen. Due to the shape of the melt

pool, quantification of the diameter of the central area visible in the vertical cross-sections was not attempted in this work, as the measured diameter depends on the z-position.

Lattice mechanical properties

Table 4 shows the measured relative densities (in %) for all combinations of lattice type and laser parameters, averaged from 3 lattice samples each. The relative densities obtained are subject to errors induced by not accounting for geometrical inaccuracies
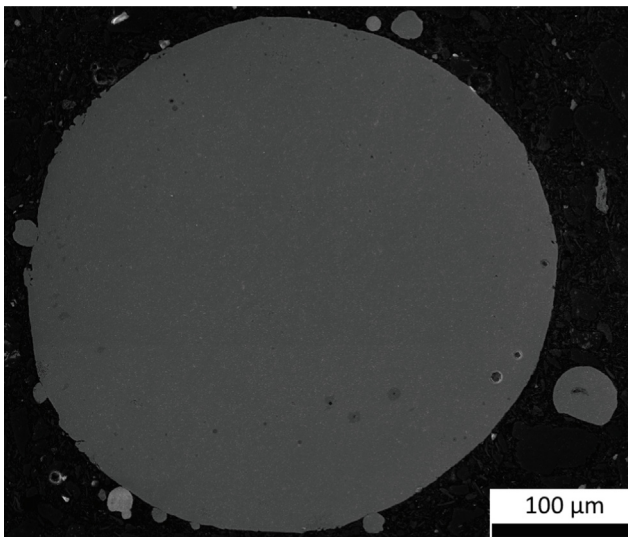
Fig. 12. SEM image of a vertical 300_30 strut in the non-etched state. Manufacturing induced porosity is still visible but significantly reduced compared to the etched state.

Table 4
Measured relative densities (in [%]) of tested lattice samples.

	200_30	200_50	300_30	300_50
f2ccz	3.7 ± 0.2	3.6 ± 0.0	6.9 ± 0.1	6.4 ± 0.1
f2cc	3.5 ± 0.2	3.2 ± 0.1	6.1 ± 0.1	5.5 ± 0.1
bcc	4.5 ± 0.1	4.2 ± 0.1	7.9 ± 0.0	6.9 ± 0.5

induced by manufacturing or sample preparation, as well as powder adhesions. The largest relative error of 7.2 % in the case of bcc 300_50 is a result of missing individual struts on the perimeter of 2 of the 3 samples.

Stress–strain curves for f2ccz 300_30 samples in the as built state, as well as bcc samples in the 350 °C heat treated state, obtained from preliminary tests are shown in Fig. 14. It can be seen that the scatter between the different tests is small. In the case of the bcc samples the standard deviation of the plateau stress is on the order of magnitude of 1 MPa, which is significantly lower than the influence of the strut diameter, as seen in Fig. 8. The same has been observed for other parameter sets. Therefore, a single representative curve for each combination of lattice geometry, laser parameters and heat treatment state was deemed sufficient for this study.

A comparison of the different tested lattice geometries in the as built state can be seen in Fig. 15. The f2ccz lattice has the highest specific strength, followed by f2cc. All samples show brittle failure via the crushing of unit cells located in shear bands. Shear bands

are initiated by struts fracturing in close proximity to the nodes. This is in line with literature, where crack initiation near nodes due to the tensile component of bending loads has been reported [17,53,88]. In the case of the f2ccz structure, the failure of the face-centered struts is preceded by the buckling and fracture of vertical struts aligned with the loading direction. The collapse of a shear band is followed by a significant stress drop. Most unit cells therefore still remain undeformed at high strains.

It can also be seen that the strain to initial failure is the lowest for f2ccz and the highest for the bcc lattice with f2cc sitting in between. It is possible that this is the result of the different inclinations of load-bearing struts. When the vertical struts in the f2ccz structure buckle or bend they rapidly lose their load-bearing capacity, resulting in failure at comparatively low strains, while bcc struts bend in an s-shape and fail more gradually.

The German norm DIN 50134 for compression testing of cellular metallic materials [91] recommends a sample size of at least 50x50 mm in the X and Y direction and a height of 100 mm. However, previous studies showed that sample sizes in the range of 5x5x5 unit cells are sufficient for testing and comparison to real world components, i.e. sandwich panels [82,92].

Fig. 16 shows the influence of process parameters on the stress–strain curves of f2cc and f2ccz lattice samples in the 350 °C heat treatment state. The same trends seen for bcc samples can also be observed here. An increase in laser power leads to higher specific strength as a result of the increased strut diameter while a change in overlap is expected to have only a minor influence. The large scatter of the f2ccz curves can potentially be attributed to a higher sensitivity of the geometry to misalignment induced by manufacturing defects or sample preparation.

Fig. 17 shows the normalized peak strength of the tested lattices in the as built state. It can be seen that the obtained data is in good agreement with values reported by Maconachie [46] and Vrána [26]. Density normalization of literature data was performed by the authors.
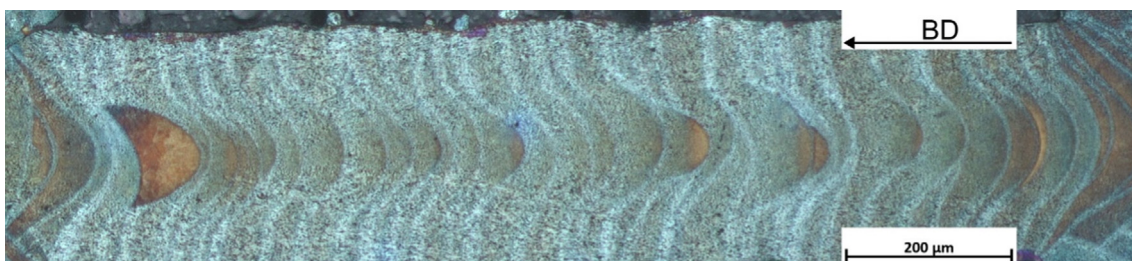

Fig. 13. Optical micrograph of the cross-section of an etched vertical strut in the as built state (build direction towards the left).
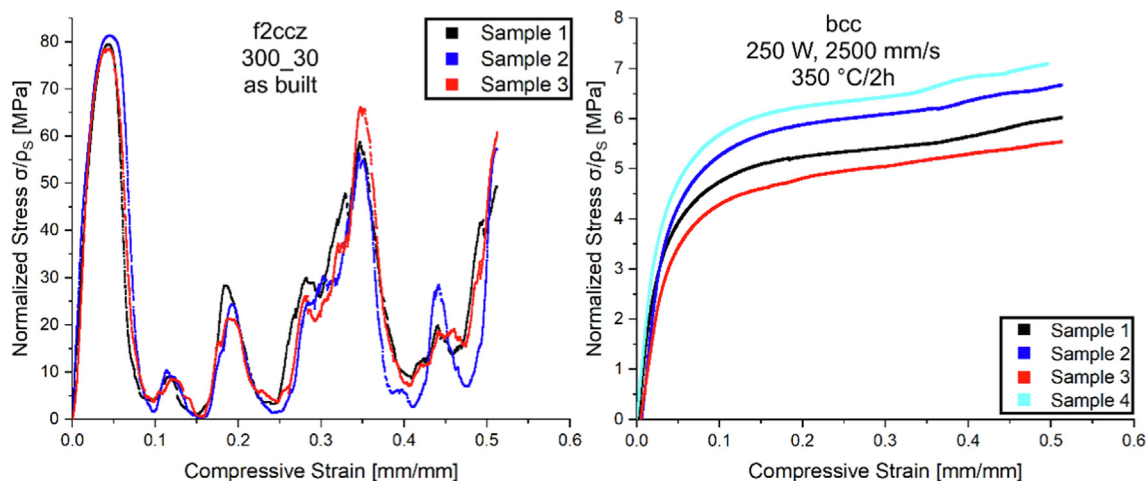
Fig. 14. Stress–strain curves for f2ccz 300_30 samples in the as built state and heat treated bcc samples manufactured with a laser power of 250 W and a scanning speed of 2500 mm/s (resulting strut diameter 290 μm and ρ_S = 4.1 %), highlighting the reproducibility of the results obtained from compression tests.
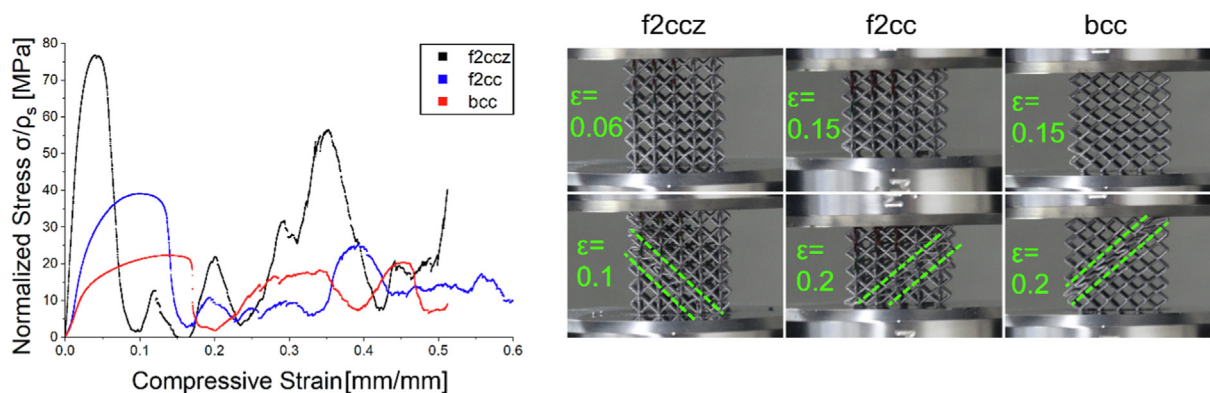

Fig. 15. Normalized stress–strain-curves and images of lattice samples manufactured with 30 % overlap and 300 W laser power in the as built state.
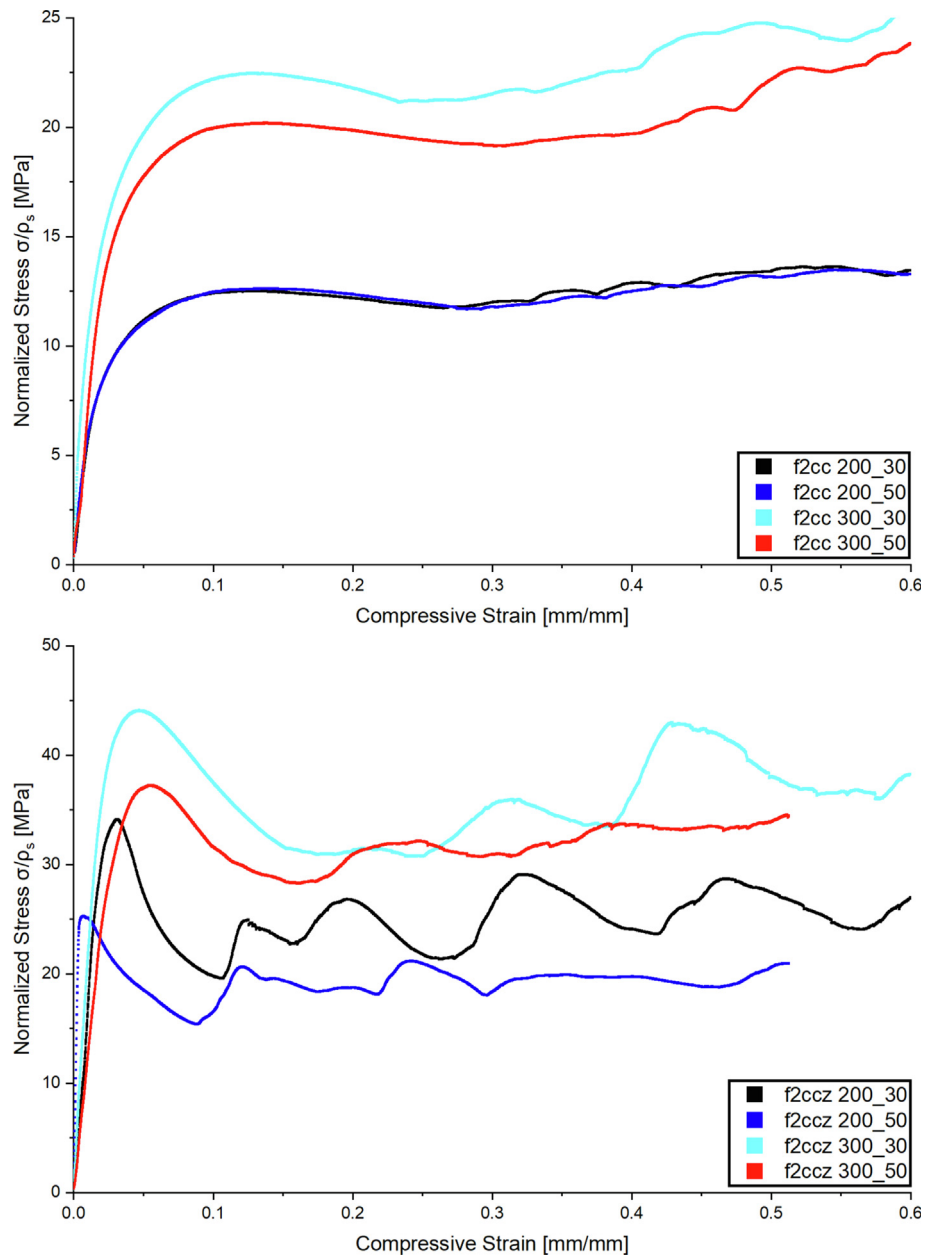
Fig. 16. Normalized stress–strain curves of f2cc (top) and f2ccz (bottom) lattice samples after the 350 °C heat treatment.
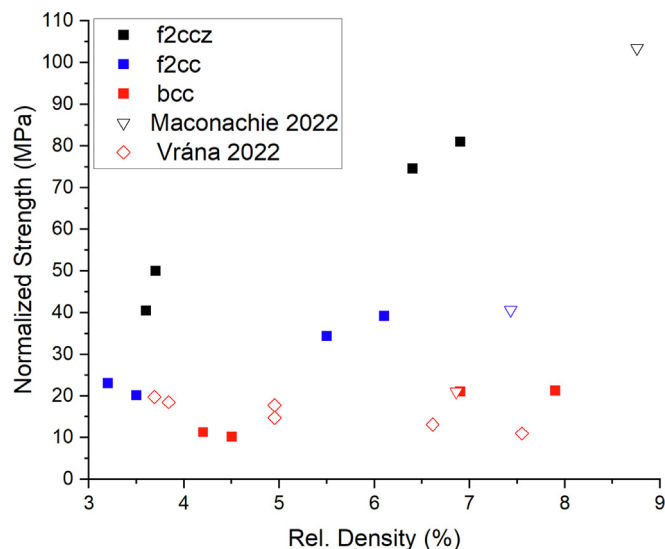
Fig. 17. Normalized compressive strength of the tested lattice geometries in the as built state as a function of relative density.

A comparison of the obtained results with literature is generally challenging, given that only limited data is available for the specific combinations of material, lattice geometry, relative density range and heat treatment state.

References

[1] B. Blakey-Milner et al., Metal additive manufacturing in aerospace: A review, Mater. Des. 209 (2021), https://doi.org/10.1016/j.matdes.2021.110008 110008.

[2] A. Kanyilmaz et al., Role of metal 3D printing to increase quality and resource-efficiency in the construction sector, Addit. Manuf. 50 (2022), https://doi.org/10.1016/j.addma.2021.102541 102541.

[3] M. Helou, S. Kara, Design, analysis and manufacturing of lattice structures: an overview, Int. J. Computer Integr. Manuf. 31 (3) (2018) 243–261, https://doi.org/10.1080/0951192X.2017.1407456.

[4] J.R. Greer, V.S. Deshpande, Three-dimensional architected materials and structures: Design, fabrication, and mechanical behavior, MRS Bull. 44 (10) (2019) 750–757, https://doi.org/10.1557/mrs.2019.232.

[5] L.-Y. Chen et al., Additive manufacturing of metallic lattice structures: Unconstrained design, accurate fabrication, fascinated performances, and challenges, Mater. Sci. Eng., R 146 (2021), https://doi.org/10.1016/j.mser.2021.100648 100648.

[6] M. Benedetti et al., Architected cellular materials: A review on their mechanical properties towards fatigue-tolerant design and fabrication, Mater. Sci. Eng., R 144 (2021), https://doi.org/10.1016/j.mser.2021.100606 100606.

[7] C.W. Isaac, F. Duddeck, Current trends in additively manufactured (3D printed) energy absorbing structures for crashworthiness application – a review, Virtual Phys. Prototyping 17 (4) (2022) 1058–1101, https://doi.org/10.1080/17452759.2022.2074698.

[8] A.E. Medvedev et al., Perspectives on additive manufacturing for dynamic impact applications, Mater. Des. 221 (2022), https://doi.org/10.1016/j.matdes.2022.110963 110963.

[9] T. Maconachie et al., SLM lattice structures: Properties, performance, applications and challenges, Mater. Des. 183 (2019), https://doi.org/10.1016/j.matdes.2019.108137 108137.

[10] A. Du Plessis et al., Properties and applications of additively manufactured metallic cellular materials: A review, Prog. Mater Sci. 125 (2022), https://doi.org/10.1016/j.pmatsci.2021.100918 100918.

[11] L. Thijs et al., Fine-structured aluminium products with controllable texture by selective laser melting of pre-alloyed AlSi10Mg powder, Acta Mater. 61 (5) (2013) 1809–1819, https://doi.org/10.1016/j.actamat.2012.11.052.

[12] T. Kurzynowski et al., Correlation between process parameters, microstructure and properties of 316 L stainless steel processed by selective laser melting, Mater. Sci. Eng. A 718 (2018) 64–73, https://doi.org/10.1016/j.msea.2018.01.103.

[13] R. Gotoh et al., Experimental and analytical investigations of AlSi10Mg, stainless steel, Inconel 625 and Ti-6Al-4V porous materials printed via powder bed fusion, Prog. Addit. Manuf. (Progress in Additive Manufacturing) 7 (5) (2022) 943–955, https://doi.org/10.1007/s40964-022-00269-8.

[14] M.J. Heiden et al., Process and feedstock driven microstructure for laser powder bed fusion of 316L stainless steel, Materialia 21 (2022), https://doi.org/10.1016/j.mtla.2022.101356 101356.

[15] K. Ishfaq, M. Abdullah, M.A. Mahmood, A state-of-the-art direct metal laser sintering of Ti6Al4V and AlSi10Mg alloys: Surface roughness, tensile strength, fatigue strength and microstructure, Opt. Laser Technol. 143 (2021), https://doi.org/10.1016/j.optlastec.2021.107366 107366.

[16] A. Du Plessis, I. Yadroitsava, I. Yadroitsev, Effects of defects on mechanical properties in metal additive manufacturing: A review focusing on X-ray tomography insights, Mater. Des. 187 (2020), https://doi.org/10.1016/j.matdes.2019.108385 108385.

[17] C. Qiu et al., Influence of processing conditions on strut structure and compressive properties of cellular lattice structures fabricated by selective laser melting, Mater. Sci. Eng. A 628 (2015) 188–197, https://doi.org/10.1016/j.msea.2015.01.031.

[18] L. Liu et al., Elastic and failure response of imperfect three-dimensional metallic lattices: the role of geometric defects induced by Selective Laser Melting, J. Mech. Phys. Solids 107 (2017) 160–184, https://doi.org/10.1016/j.jmps.2017.07.003.

[19] A. Großmann, J. Gosmann, C. Mittelstedt, Lightweight lattice structures in selective laser melting: Design, fabrication and mechanical properties, Mater. Sci. Eng. A 766 (2019), https://doi.org/10.1016/j.msea.2019.138356 138356.

[20] A.D. Dressler et al., Heterogeneities dominate mechanical performance of additively manufactured metal lattice struts, Addit. Manuf. 28 (2019) 692–703, https://doi.org/10.1016/j.addma.2019.06.011.

[21] M. Leary et al., Selective laser melting (SLM) of AlSi12Mg lattice structures, Mater. Des. 98 (2016) 344–357, https://doi.org/10.1016/j.matdes.2016.02.127.

[22] M. Leary et al., Inconel 625 lattice structures manufactured by selective laser melting (SLM): Mechanical properties, deformation and failure modes, Mater. Des. 157 (2018) 179–199, https://doi.org/10.1016/j.matdes.2018.06.010.

[23] G. Meyer et al., Manufacturability investigation of inclined AlSi10Mg lattice struts by means of selective laser melting, Manuf. Lett. 31 (2022) 101–105, https://doi.org/10.1016/j.mfglet.2021.08.002.

[24] C. López-García et al., A dimensional assessment of small features and lattice structures manufactured by laser powder bed fusion, Prog. Addit. Manuf. (Progress in Additive Manufacturing) 7 (4) (2022) 751–763, https://doi.org/10.1007/s40964-022-00263-0.

[25] S.A. Naghavi et al., On the Morphological Deviation in Additive Manufacturing of Porous Ti6Al4V Scaffold: A Design Consideration, Materials 15 (14) (2022), https://doi.org/10.3390/ma15144729.

[26] R. Vrána et al., Deviations of the SLM Produced Lattice Structures and Their Influence on Mechanical Properties, Materials 15 (9) (2022) 3144, https://doi.org/10.3390/ma15093144.

[27] X.Z. Zhang et al., Additive manufacturing of intricate lattice materials: Ensuring robust strut additive continuity to realize the design potential, Addit. Manuf. 58 (2022), https://doi.org/10.1016/j.addma.2022.103022 103022.

[28] P. Delroisse et al., Effect of strut orientation on the microstructure heterogeneities in AlSi10Mg lattices processed by selective laser melting, Scr. Mater. 141 (2017) 32–35, https://doi.org/10.1016/j.scriptamat.2017.07.020.

[29] Z. Dong et al., Study of Size Effect on Microstructure and Mechanical Properties of AlSi10Mg Samples Made by Selective Laser Melting, Materials 11 (12) (2018), https://doi.org/10.3390/ma11122463.

[30] N. Takata et al., Size dependence of microstructure of AlSi10Mg alloy fabricated by selective laser melting, Mater. Charact. 143 (2018) 18–26, https://doi.org/10.1016/j.matchar.2017.11.052.

[31] Z. Dong et al., Orientation dependency for microstructure, geometric accuracy and mechanical properties of selective laser melting AlSi10Mg lattices, J. Alloys Compd. 791 (2019) 490–500, https://doi.org/10.1016/j.jallcom.2019.03.344.

[32] Z. Dong et al., Microstructural heterogeneity of AlSi10Mg alloy lattice structures fabricated by selective laser melting: Phenomena and mechanism, J. Alloys Compd. 833 (2020), https://doi.org/10.1016/j.jallcom.2020.155071 155071.

[33] G. Meyer et al., Influence of the Miniaturisation Effect on the Effective Stiffness of Lattice Structures in Additive Manufacturing, Metals 10 (11) (2020) 1442, https://doi.org/10.3390/met10111442.

[34] S.I. Shahabad et al., On the effect of thin-wall thickness on melt pool dimensions in laser powder-bed fusion of Hastelloy X: Numerical modeling and experimental validation, J. Manuf. Processes 75 (2022) 435–449, https://doi.org/10.1016/j.jmapro.2022.01.029.

[35] R. Vrána et al., Selective Laser Melting Strategy for Fabrication of Thin Struts Usable in Lattice Structures, Materials 11 (9) (2018), https://doi.org/10.3390/ma11091763.

[36] O. Poncelet et al., Critical assessment of the impact of process parameters on vertical roughness and hardness of thin walls of AlSi10Mg processed by laser powder bed fusion, Addit. Manuf. 38 (2021), https://doi.org/10.1016/j.addma.2020.101801 101801.

[37] M. Sairaiji et al., Effect of Scan Strategy on Mechanical Properties of AlSi12 Lattice Fabricated by Selective Laser Melting, J. Laser Micro/Nanoeng. (2020), https://doi.org/10.2961/jlmn.2020.01.2002.

[38] F. Guaglione et al., Single point exposure LPBF for the production of biodegradable Zn-alloy lattice structures, Addit. Manuf. 48 (2021), https://doi.org/10.1016/j.addma.2021.102426 102426.

[39] B.B. Babamiri, J.R. Mayeur, K. Hazeli, Synchronous involvement of topology and microstructure to design additively manufactured lattice structures, Addit. Manuf. 52 (2022), https://doi.org/10.1016/j.addma.2022.102618 102618.

[40] A. Bertocco et al., Lattice structures in stainless steel 17–4PH manufactured via selective laser melting (SLM) process: dimensional accuracy, satellites formation, compressive response and printing parameters optimization, Int. J. Adv. Manuf. Technol. 120 (7–8) (2022) 4935–4949, https://doi.org/10.1007/s00170-022-08946-2.

[41] J. Noronha et al., Additive manufacturing of Ti-6Al-4V horizontal hollow struts with submillimetre wall thickness by laser powder bed fusion, Thin-Walled Struct. 179 (2022), https://doi.org/10.1016/j.tws.2022.109620 109620.

[42] E. Abele et al., Optimisation of process parameters for lattice structures, Rapid Prototyp. J. (Rapid Prototyping Journal) 21 (1) (2015) 117–127, https://doi.org/10.1108/RPJ-10-2012-0096.

[43] R. Vrána et al., Contour laser strategy and its benefits for lattice structure manufacturing by selective laser melting technology, J. Manuf. Processes 74 (2022) 640–657, https://doi.org/10.1016/j.jmapro.2021.12.006.

[44] D.S. Al-Saedi et al., Mechanical properties and energy absorption capability of functionally graded F2BCC lattice fabricated by SLM, Mater. Des. 144 (2018) 32–44, https://doi.org/10.1016/j.matdes.2018.01.059.

[45] I. Maskery et al., A mechanical property evaluation of graded density Al-Si10-Mg lattice structures manufactured by selective laser melting, Mater. Sci. Eng. A 670 (2016) 264–274, https://doi.org/10.1016/j.msea.2016.06.013.

[46] T. Maconachie et al., The effect of topology on the quasi-static and dynamic behaviour of SLM AlSi10Mg lattice structures, Int. J. Adv. Manuf. Technol. 118 (11–12) (2022) 4085–4104, https://doi.org/10.1007/s00170-021-08203-y.

[47] J. Jung et al., Load Introduction Specimen Design for the Mechanical Characterisation of Lattice Structures under Tensile Loading, J. Manuf. Mater. Process. 7 (1) (2023) 37, https://doi.org/10.3390/jmmp7010037.

[48] EOS GmbH. Aluminium AlSi10Mg Material Data Sheet. [June 20, 2022]; Available from: https://www.eos.info/03_system-related-assets/material-related-contents/metal-materials-and-examples/metal-material-datasheet/aluminium/material_datasheet_eos_aluminium-alsi10mg_en_web.pdf.

[49] A. Großmann et al., Melt pool controlled laser powder bed fusion for customised low-density lattice structures, Mater. Des. 181 (2019), https://doi.org/10.1016/j.matdes.2019.108054 108054.

[50] G. Meyer, Influence of the miniaturization effect on lattice structures by means of PBF with AlSi10Mg, MSE Congress (2020).

[51] M. Liu et al., Effect of Heat Treatment on Gradient Microstructure of AlSi10Mg Lattice Structure Manufactured by Laser Powder Bed Fusion, Materials 13 (11) (2020), https://doi.org/10.3390/ma13112487.

[52] L. Zhuo et al., Effect of post-process heat treatment on microstructure and properties of selective laser melted AlSi10Mg alloy, Mater. Lett. 234 (2019) 196–200, https://doi.org/10.1016/j.matlet.2018.09.109.

[53] A. Suzuki et al., Effects of Heat Treatments on Compressive Deformation Behaviors of Lattice-Structured AlSi10Mg Alloy Fabricated by Selective Laser Melting, Adv. Eng. Mater. 21 (10) (2019) 1900571, https://doi.org/10.1002/adem.201900571.

[54] Q. Han, Y. Jiao, Effect of heat treatment and laser surface remelting on AlSi10Mg alloy fabricated by selective laser melting, Int. J. Adv. Manuf. Technol. 102 (9–12) (2019) 3315–3324, https://doi.org/10.1007/s00170-018-03272-y.

[55] EDAX. Product Bulletin - NPAR. [August 15, 2022]; Available from: https://www.edax.com/-/media/ametekedax/files/ebsd/product_bulletins/npar_pb.pdf.

[56] N. Takata et al., Change in microstructure of selectively laser melted AlSi10Mg alloy with heat treatments, Mater. Sci. Eng. A 704 (2017) 218–228, https://doi.org/10.1016/j.msea.2017.08.029.

[57] T. Maeshima, K. Oh-Ishi, Solute clustering and supersaturated solid solution of AlSi10Mg alloy fabricated by selective laser melting, Heliyon 5 (2) (2019) e01186.

[58] F. Alghamdi, M. Haghshenas, Microstructural and small-scale characterization of additive manufactured AlSi10Mg alloy. SN, Appl. Sci. 1 (3) (2019), https://doi.org/10.1007/s42452-019-0270-5.

[59] F. Alghamdi et al., Post heat treatment of additive manufactured AlSi10Mg: On silicon morphology, texture and small-scale properties, Mater. Sci. Eng. A 783 (2020), https://doi.org/10.1016/j.msea.2020.139296 139296.

[60] L. Thijs et al., Strong morphological and crystallographic texture and resulting yield strength anisotropy in selective laser melted tantalum, Acta Mater. 61 (12) (2013) 4657–4668, https://doi.org/10.1016/j.actamat.2013.04.036.

[61] S.S. Al-Bermani et al., The Origin of Microstructural Diversity, Texture, and Mechanical Properties in Electron Beam Melted Ti-6Al-4V, Metall. Mater. Trans. A 41 (13) (2010) 3422–3434, https://doi.org/10.1007/s11661-010-0397-x.

[62] F. Brenne et al., Microstructural design of Ni-base alloys for high-temperature applications: impact of heat treatment on microstructure and mechanical properties after selective laser melting, Prog. Addit. Manuf. 1 (3–4) (2016) 141–151, https://doi.org/10.1007/s40964-016-0013-8.

[63] T. Niendorf, F. Brenne, M. Schaper, Lattice Structures Manufactured by SLM: On the Effect of Geometrical Dimensions on Microstructure Evolution During Processing, Metall. Mater. Trans. B 45 (4) (2014) 1181–1185, https://doi.org/10.1007/s11663-014-0086-z.

[64] T. Niendorf et al., Microstructural Evolution and Functional Properties of Fe-Mn-Al-Ni Shape Memory Alloy Processed by Selective Laser Melting, Metall. Mater. Trans. A 47 (6) (2016) 2569–2573, https://doi.org/10.1007/s11661-016-3412-z.

[65] G. Reinhart, S. Teufelhart, F. Riss, Investigation of the Geometry-Dependent Anisotropic Material Behavior of Filigree Struts in ALM-Produced Lattice Structures, Phys. Procedia 39 (2012) 471–479, https://doi.org/10.1016/j.phpro.2012.10.063.

[66] Y.J. Liu et al., Gradient in microstructure and mechanical property of selective laser melted AlSi10Mg, J. Alloys Compd. 735 (2018) 1414–1421, https://doi.org/10.1016/j.jallcom.2017.11.020.

[67] W. Li et al., Effect of heat treatment on AlSi10Mg alloy fabricated by selective laser melting: Microstructure evolution, mechanical properties and fracture mechanism, Mater. Sci. Eng. A 663 (2016) 116–125, https://doi.org/10.1016/j.msea.2016.03.088.

[68] F. Trevisan et al., On the Selective Laser Melting (SLM) of the AlSi10Mg Alloy: Process, Microstructure, and Mechanical Properties, Materials 10 (1) (2017), https://doi.org/10.3390/ma10010076.

[69] I. Rosenthal, A. Stern, N. Frage, Microstructure and Mechanical Properties of AlSi10Mg Parts Produced by the Laser Beam Additive Manufacturing (AM) Technology, Metallogr. Microstruct. Anal. 3 (6) (2014) 448–453, https://doi.org/10.1007/s13632-014-0168-y.

[70] M. Tang et al., Rapid Solidification: Selective Laser Melting of AlSi10Mg, JOM 68 (3) (2016) 960–966, https://doi.org/10.1007/s11837-015-1763-3.

[71] Y. Li, D. Gu, Parametric analysis of thermal behavior during selective laser melting additive manufacturing of aluminum alloy powder, Mater. Des. 63 (2014) 856–867, https://doi.org/10.1016/j.matdes.2014.07.006.

[72] S.P. Narra, L. Scime, J. Beuth, Integrated Control of Melt Pool Geometry and Microstructure in Laser Powder Bed Fusion of AlSi10Mg, Metall. Mater. Trans. A 49 (10) (2018) 5097–5106, https://doi.org/10.1007/s11661-018-4804-z.

[73] Y. AbouelNour, N. Gupta, In-situ monitoring of sub-surface and internal defects in additive manufacturing: A review, Mater. Des. 222 (2022), https://doi.org/10.1016/j.matdes.2022.111063 111063.

[74] C. Zhang et al., The Effect of Annealing on Microstructure and Mechanical Properties of Selective Laser Melting AlSi10Mg, IOP Conf. Ser.: Mater. Sci. Eng. 538 (1) (2019), https://doi.org/10.1088/1757-899X/538/1/012023.

[75] P. Snopiński et al., Effects of equal channel angular pressing and heat treatments on the microstructures and mechanical properties of selective laser melted and cast AlSi10Mg alloys, Archiv. Civ. Mech. Eng. (Archives of Civil and Mechanical Engineering) 21 (3) (2021), https://doi.org/10.1007/s43452-021-00246-y.

[76] P. Snopiński et al., Evolution of Microstructure, Texture and Corrosion Properties of Additively Manufactured AlSi10Mg Alloy Subjected to Equal Channel Angular Pressing (ECAP), Symmetry 14 (4) (2022) 674, https://doi.org/10.3390/sym14040674.

[77] J. Gurland, The measurement of grain contiguity in two-phase alloys, Trans. Metall. Soc. AIME 212 (1958) 452–455.

[78] J. Fiocchi et al., Low temperature annealing dedicated to AlSi10Mg selective laser melting products, J. Alloys Compd. 695 (2017) 3402–3409, https://doi.org/10.1016/j.jallcom.2016.12.019.

[79] Y. Shen et al., The Mechanical Properties of Sandwich Structures Based on Metal Lattice Architectures, J. Sandw. Struct. Mater. 12 (2) (2010) 159–180, https://doi.org/10.1177/1099636209104536.

[80] R. Gümrük, R. Mines, S. Karadeniz, Static mechanical behaviours of stainless steel micro-lattice structures under different loading conditions, Mater. Sci. Eng. A 586 (2013) 392–406, https://doi.org/10.1016/j.msea.2013.07.070.

[81] R. Gümrük, R. Mines, Compressive behaviour of stainless steel micro-lattice structures, Int. J. Mech. Sci. 68 (2013) 125–139, https://doi.org/10.1016/j.ijmecsci.2013.01.006.

[82] B. Gorny et al., In situ characterization of the deformation and failure behavior of non-stochastic porous structures processed by selective laser melting, Mater. Sci. Eng. A 528 (27) (2011) 7962–7967, https://doi.org/10.1016/j.msea.2011.07.026.

[83] Y. Bian et al., Similarities of the Mechanical Responses of Body-Centered Cubic Lattice Structures with Different Constituent Materials Under Compression, JOM 74 (4) (2022) 1774–1783, https://doi.org/10.1007/s11837-021-04926-1.

[84] H.A. AlQaydi et al., Hybridisation of AlSi10Mg lattice structures for engineered mechanical performance, Addit. Manuf. 57 (2022), https://doi.org/10.1016/j.addma.2022.102935 102935.

[85] Q. Sun et al., Investigation on Mechanical Properties and Energy Absorption Capabilities of AlSi10Mg Triply Periodic Minimal Surface Sheet Structures Fabricated via Selective Laser Melting, J. Mater. Eng. Perform. (2022), https://doi.org/10.1007/s11665-022-06883-5.

[86] O. Al-Ketan, D.-W. Lee, A.-R. Abu, K., Mechanical properties of additively-manufactured sheet-based gyroidal stochastic cellular materials, Addit. Manuf. 48 (2021), https://doi.org/10.1016/j.addma.2021.102418 102418.

[87] C. Peng, P. Marzocca, P. Tran, Triply periodic minimal surfaces based honeycomb structures with tuneable mechanical responses, Virtual Phys. Prototyping 18 (1) (2022), https://doi.org/10.1080/17452759.2022.2125879.

[88] X. Liu et al., Understanding and suppressing shear band formation in strut-based lattice structures manufactured by laser powder bed fusion, Mater. Des. 199 (2021), https://doi.org/10.1016/j.matdes.2020.109416 109416.

[89] H.L. Fan, D.N. Fang, F.N. Jing, Yield surfaces and micro-failure mechanism of block lattice truss materials, Mater. Des. 29 (10) (2008) 2038–2042, https://doi.org/10.1016/j.matdes.2008.04.013.

[90] S. Banait et al., Coupled effect of microstructure and topology on the mechanical behavior of Inconel718 additively manufactured lattices, Mater. Des. 224 (2022), https://doi.org/10.1016/j.matdes.2022.111294 111294.

[91] [DIN 50134] Prüfung von metallischen Werkstoffen: Druckversuch an metallischen zellularen Werkstoffen;77.040.10; 2008.

[92] F. Brenne, T. Niendorf, H.J. Maier, Additively manufactured cellular structures: Impact of microstructure and local strains on the monotonic and cyclic behavior under uniaxial and bending load, J. Mater. Process. Technol. 213 (9) (2013) 1558–1564, https://doi.org/10.1016/j.jmatprotec.2013.03.013.